Corrosion Science 187 (2021) 109479

Contents lists available at ScienceDirect

Corrosion Science

journal homepage: www.elsevier.com/locate/corsci

$Al_xCoCrFeNi$ high entropy alloys with superior hot corrosion resistance to Na_2SO_4 + 25% NaCl at 900 °C

Ling Li [a], Jie Lu [a], Xuanzhen Liu [a], Tao Dong [b], Xiaofeng Zhao [a,*], Fan Yang [c,*], Fangwei Guo [a]

[a] Shanghai Key Laboratory of Advanced High-Temperature Materials and Precision Forming, School of Materials Science and Engineering, Shanghai Jiao Tong University, Shanghai, 200240, China
[b] Yantai Research Institute and Graduate School, Harbin Engineering University, Yantai, 265500, China
[c] School of Mechanical Engineering, Shanghai Jiao Tong University, Shanghai, 200240, China

ARTICLE INFO

Keywords:
Hot corrosion
High entropy alloy
AlCoCrFeNi
Coherent interface

ABSTRACT

Hot corrosion behaviors of Y, Hf-codoped $Al_xCoCrFeNi$ (Al_x, x = 0.7, 1.0, and 1.3) high-entropy alloys (HEAs) under Na_2SO_4 + 25 % NaCl molten salts at 900 °C were investigated and compared with those of the conventional NiCoCrAl alloy. The results show $Al_{1.0}$ and $Al_{1.3}$ with spinodally decomposed structure of A2 + B2 phases possess significantly enhanced hot corrosion resistance than $Al_{0.7}$ with eutectic lamellar structure and NiCoCrAl. The superior hot corrosion resistance is attributed to the loop-locked coherent phase interfaces in the modulated structure, along with the improved availability of Al and the high Cr content.

1. Introduction

Hot section components of a gas turbine engine are exposed to harsh environments such as hot gas stream with corrosive species. Driven by the demand for enhanced energy efficiency and minimum emission of pollutants, the future engine has to work under a higher operating temperature and sometimes in more aggressive environments, which puts forward higher requirements on the hot corrosion resistance of materials [1]. Hot corrosion is accelerated oxidation induced by salt contaminants such as Na_2SO_4, NaCl, and V_2O_5 depositing on the surface of the turbine blade [2–4]. Na_2SO_4 is the main deposit, which is formed by the reaction between the oxidation products of sulfur in the fossil fuel (SO_2/SO_3) and NaCl aerosol in the atmosphere [3–5]. If operating under marine environment, NaCl ingested by the engine plays a critical role by decreasing the melting point of eutectic mixtures with Na_2SO_4 to 620 °C and accelerating hot corrosion by forming volatile metal chloride [2,6].

Nickel-based superalloy is widely used in gas turbine engines. To maintain its excellent high-temperature creep strength, Al and Cr, the two elements offering resistances to oxidation and hot corrosion respectively, must be kept in a low concentration [7]. Therefore, oxidation- and corrosion-resistant coatings are usually applied to protect the superalloy. MCrAlY (M = Ni and/or Co) coatings, which have a good balance among oxidation resistance, hot corrosion resistance, and ductility, have been widely used as standalone overlayers and bond coat in thermal barrier coatings (TBCs). Researchers have made lots of efforts to improve the hot corrosion performance of MCrAlY coatings by adding modification elements such as Si [8], Ta [9,10], Re [11], Pt [12], or by designing novel structure such as SMARTCOAT [13], nanocrystalline coating [14] and Al gradient structure [15].

AlCoCrFeNi, a type of high-entropy alloys (HEAs), has attracted considerable interest due to its adjustable microstructure and excellent mechanical properties [16–18]. With high levels of Al and Cr, AlCoCrFeNi HEAs are expected to have high resistance to both oxidation and hot corrosion. Tsao et al. [19] investigated the type-I hot corrosion performance of NiCoFeAlCrTi HEAs against Na_2SO_4 + 25 % NaCl by both salt-coated and crucible tests and suggested that high Cr content is beneficial to hindering hot corrosion attack and internal sulfidation. Butler et al. [20,21] investigated the high-temperature oxidation behaviors of AlCoCrFeNi at 1050 °C and found the HEA formed a combination of AlN and Al_2O_3 beneath an external Cr_2O_3 scale. It has been demonstrated in our recent work that Y, Hf-codoped $Al_xCoCrFeNi$ HEAs have excellent oxidation and spallation resistance at 1100 °C with low parabolic rate constants for about 2×10^{-13} $g^2\,cm^{-4}s^{-1}$ at 1100 °C, which is the same order of magnitude as NiAlHf and RE doped FeCrAl [22–24]. It is therefore interesting to investigate the hot corrosion behaviors of Y, Hf-codoped AlCoCrFeNi HEAs and to reveal the underlying corrosion mechanism(s).

Here we prepared Y, Hf-codoped $Al_xCoCrFeNi$ (x = 0.7, 1.0 and 1.3)

* Corresponding authors.
E-mail addresses: xiaofengzhao@sjtu.edu.cn (X. Zhao), fanyang_0123@sjtu.edu.cn (F. Yang).

https://doi.org/10.1016/j.corsci.2021.109479
Received 6 December 2020; Received in revised form 14 April 2021; Accepted 17 April 2021
Available online 20 April 2021

HEAs by arc-melting and investigated Type-I hot corrosion behaviors of these alloys under mixed salts (75 wt % Na_2SO_4 + 25 wt % NaCl) at 900 °C. The conventional NiCoCrAl alloy was also studied for comparison. Results show HEAs with spinodally decomposed structure possess superior hot corrosion resistance. They also have excellent performances to defend internal sulfidation and oxidation, as well as to maintain the integrity of the alloys after long-time hot corrosion. Results from this work provide a new insight into the design of hot corrosion resistant materials and shed light on the potential application of AlCoCrFeNi as hot corrosion resistant coating, bond coat in TBCs, and structural-functional integrated alloy working at high-temperature.

2. Material

2.1. Materials preparation

Al_xCoCrFeNi (x = 0.7, 1.0, and 1.3) HEAs were prepared by arc-melting. NiCoCrAl with the same elemental composition as commercial Amdry 365, Oerlikon Metco, was also prepared for comparison. All the alloys were doped with 0.05 % Y and 0.05 % Hf. The specific chemical compositions for the as-cast alloys are listed in Table 1.

The above cast alloys were prepared by arc-melting the mixture of the high pure metals (99.99 wt %) in water-cooled copper hearth under a Ti-gettered high-purity argon atmosphere. The ingots were flipped and remelted five times to ensure compositional homogeneity. All the as-cast ingots were homogenized at 1250 °C for 5 h in an argon atmosphere with 5 °C min^{-1} for both heating and cooling. After homogenization, cylindrical specimens (diameter of 11.5 mm and thickness of 3 mm) were cut from the ingots by wire cutting, and ground by #240, #400, #600, #800, #1000 SiC sandpapers in sequence. All samples were cleaned sequentially by deionized water, alcohol, and acetone in an ultrasonic bath for 3 min for each step before hot corrosion tests.

2.2. Hot corrosion test

The sample was heated on a 120 °C hot plate. Saturated solution of highly pure Na_2SO_4 + 25 wt % NaCl mixing salts in deionized water was sprayed to the sample surface to result in a 2.0 ± 0.1 mg cm^{-2} solid load. Subsequently, the sample was put into a crucible. A cap was applied to cover the crucible to collect the spallation of corrosion products with a minimum loss. Hot corrosion tests were carried out at 900 °C in static air in a muffle furnace with an accuracy of ±1 °C. After cooling to room-temperature, the sample was carefully removed from the crucible and soaked in 80 °C deionized water for 5 min to remove the remaining salts. Subsequently, the sample was held by a tweezer from the side and shaken gently to wash away the loose-bonded corrosion products before taking out from the water. Sample mass before and after corrosion tests, as well as the mass of spalled corrosion products collected from the crucible, were measured by an electronic balance with a sensitivity of 10^{-5} g to calculate the net and the gross mass gain (definitions are given in Section 3.2). After the mass measurement, the samples were recoated with a uniform fresh salt (2.0 ± 0.1 mg cm^{-2}) and subjected to the next round of corrosion test till 160 h.

Table 1
Nominal compositions of the four alloys.

Materials	Element (at %)						
	Al	Co	Cr	Fe	Ni	Y	Hf
$Al_{0.7}$	14.9	21.3	21.3	21.3	21.3	0.05	0.05
$Al_{1.0}$	20.0	20.0	20.0	20.0	20.0	0.05	0.05
$Al_{1.3}$	24.5	18.9	18.9	18.9	18.9	0.05	0.05
NiCoCrAl	22.5	19.7	16.5	/	41.3	0.05	0.05

2.3. Characterizations

Microstructure and composition of the specimens before and after hot corrosion were analyzed by scanning electron microscopy (SEM, Mira3, TESCAN, Czech) equipped with energy-dispersive X-ray spectroscopy (EDS, Aztec X-MaxN80, Oxford Instruments). The phase interface of the spinodally decomposed HEAs was analyzed using a scanning transmission electron microscope (STEM, Talos F200X G2, Thermo Fisher Scientific, USA) equipped with energy-dispersive X-ray spectroscopy (EDS) system on the thin lamella of $Al_{1.3}$ prepared by a focused ion beam (FIB, GAIA3, TESCAN, Czech).

The semi-quantitative depth profiles of O, S, and Na were characterized by radiofrequency glow discharge optical emission spectroscopy (GD-OES, GDA750HP, Spectruma Analytik GmbH, Germany) with the sample not washed after the last corrosion cycle at 160 h. The mass change was measured by an electronic balance (DV215CD, OHAUS, USA) with a precision of 10^{-5} g. The phase of the surface after hot corrosion was identified by X-ray diffraction with a 6 mm anti-scatter slit (XRD, Ultima IV, Rigaku, Japan). Volume fraction of each phase in the alloys and ratios of spallation/spinel to the whole surface were obtained by image analysis using Image J software.

3. Results

3.1. Microstructure of HEAs before hot corrosion

Microstructure of the Al_xCoCrFeNi (x = 0.7, 1.0, and 1.3) HEAs and the NiCoCrAl alloy before hot corrosion is presented in Fig. 1. $Al_{0.7}$ is a eutectic alloy with a face-centered cubic (A1) and ordered body-centered cubic (B2) two-phase lamellar microstructure [24,25] (Fig. 1a). Laths in different areas are aligned along with different directions with parallel phase interfaces among the laths in each area. $Al_{1.0}$ and $Al_{1.3}$ show a spinodally decomposed two-phase structure with FeCr body-centered cubic (A2) phase particles dispersed in the B2 β-NiAl phase (Fig. 1b and 1c) [18]. The particles in $Al_{1.3}$ and $Al_{1.0}$ are both micron to submicron in size, but an apparent reduction of particle size can be observed with increasing x. NiCoCrAl alloy consists of coarse A1 γ-Ni phase and a large number of needle-like, fine γ phases precipitate in the B2 β-NiAl matrix. The chemical composition and volume fractions of each phase in the four alloys are listed in Table 2.

3.2. Surface morphologies and weight changes after hot corrosion

Fig. 2 shows the optical images of the sample surfaces after hot corrosion at 900 °C under Na_2SO_4 + 25 % NaCl molten salts for 0.5, 20, 60, and 160 h, where different spallation behaviors can be observed among these alloys. At the same corrosion time, spallation decreases with increasing Al content in the HEAs. For example, $Al_{1.3}$ has the fewest spallation sites with the most intact oxide scale during the whole corrosion process. A few black products formed at the sample edge can be observed after 160 h corrosion, which is later identified as $CoFe_2O_4$ spinel. $Al_{1.0}$ has similar corrosion behaviors but shows more spallation and earlier formation of spinel than $Al_{1.3}$. $Al_{0.7}$ shows complex morphologies after 160 h hot corrosion. Catastrophic spallation occurs on $Al_{0.7}$ with large flaky scales disengaged from the substrate exposing uneven surface. NiCoCrAl presents different spallation behavior with the HEAs. (Ni, Co)(Al, Cr)$_2O_4$ spinel can be observed at the very early stage of hot corrosion (0.5 h). After 20 h, ~ 45 % of the oxide scale has spalled. The remaining scales consist of (Al, Cr)$_2O_3$ and (Ni, Co)(Al, Cr)$_2O_4$ spinel. After 160 h hot corrosion, large spinel clusters are formed on the surface with bare metal besides the clusters. A spallation ratio, defined as the spalled area over the total surface area, and a spinel ratio (spinel area/total surface area) obtained from image analysis are presented in Fig. 3, where significantly lower values can be observed in $Al_{1.0}$ and $Al_{1.3}$ than $Al_{0.7}$ and NiCoCrAl.

Corrosion kinetic curves are presented in Fig. 4. Here two types of

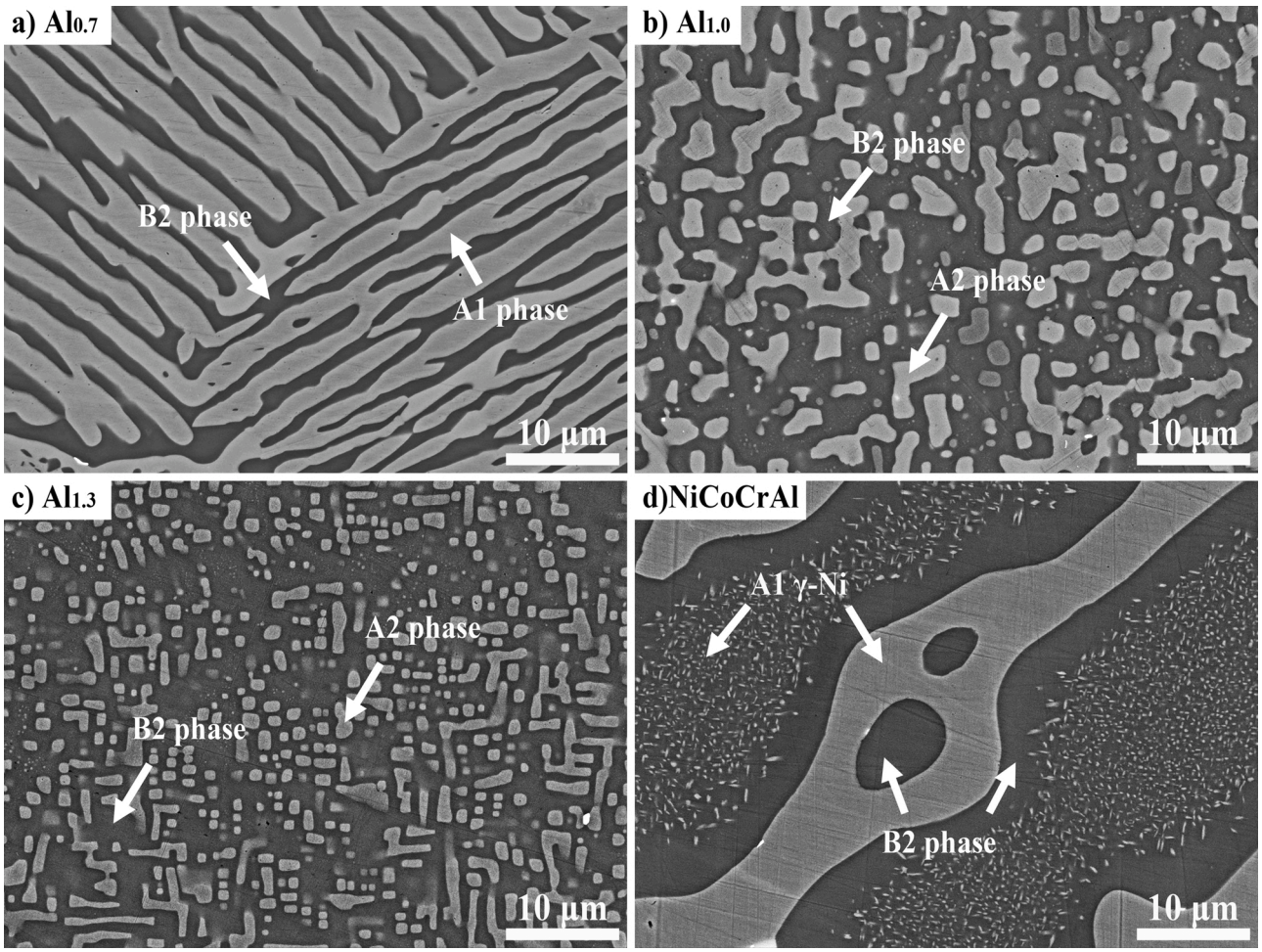

Fig. 1. Microstructure of the four alloys before corrosion tests: (a) $Al_{0.7}$, (b) $Al_{1.0}$, (c) $Al_{1.3}$ and (d) NiCoCrAl. Images were taken under back-scatter electron (BSE) mode.

Table 2
Chemical composition (at %) and volume fraction of each phase in the four alloys before corrosion tests.

Material	Phases	Volume fraction (vol %)	Element (at %)				
			Al	Co	Cr	Fe	Ni
$Al_{0.7}$	A1	64.2	4.8	24.5	28.0	27.7	15.0
	B2	35.8	33.5	16.3	6.9	11.1	32.2
$Al_{1.0}$	A2	43.9	3.3	21.3	37.7	29.2	8.5
	B2	56.1	32.8	18.8	7.7	13.6	27.1
$Al_{1.3}$	A2	26.7	4.5	16.4	45.0	29.1	5.0
	B2	73.3	33.4	19.4	9.0	14.3	23.9
NiCoCrAl	A1	42.1	7.2	30.3	30.6	/	31.9
	B2	57.9	35.6	11.5	5.7	/	47.2

mass change were used to evaluate the hot corrosion resistance of the alloys: 1) net mass gain, defined as the mass change of the alloy after hot corrosion and 2) gross mass grain, defined as the sum of net mass gain of the alloy and mass of the spalled corrosion products collected from the crucible (net mass gain + mass of spallations). As shown in Fig. 4a, $Al_{0.7}$ has the highest gross mass gain with a steady and steep increase rate after 40 h. $Al_{1.0}$ and $Al_{1.3}$ have similar gross mass gain before 100 h, but $Al_{1.0}$ shows a faster increase with time than $Al_{1.3}$ after 100 h when accelerated spallation takes place. The gross mass gain for NiCoCrAl is in between $Al_{0.7}$ and $Al_{1.0}$.

For the net mass gain, $Al_{0.7}$ has a negative value, and an accelerated mass loss during hot corrosion, as shown in Fig. 4b. Catastrophic spallation occurs after 140 h when oxidation and spallation are too severe to measure. On the contrary, the other three alloys show positive or little negative net mass gain after hot corrosion, among which $Al_{1.3}$ has the highest value.

XRD patterns of the four alloys after hot corrosion for 160 h are shown in Fig. 5. To avoid the undesirable preferential attack at edges, namely edge effects [26], only the center areas of the samples were characterized to reflect the intrinsic properties of the materials. For $Al_{0.7}$, spinel and Cr_2O_3 are the major reaction products without detection of Al_2O_3. For $Al_{1.0}$ and $Al_{1.3}$, the scales mainly consist of Cr_2O_3 and Al_2O_3. NiCoCrAl has the most complex phase composition with the presence of Al_2O_3, Cr_2O_3, and spinel.

3.3. Surface morphology after 0.5 h exposure

Surface morphologies of the alloys after hot corrosion for 0.5 h are shown in Fig. 6. For $Al_{0.7}$, a low-magnification SEM image (Fig. 6a) shows inhomogeneity both in the remaining oxide scale and the exposed metal surface after spallation. A high-magnification image of the oxide scale (Fig. 6b) shows randomly distributed particles with different sizes embedding in the oxides. EDS analyses indicate the fine, spherical particles are the $Al_{0.7}$ alloy and the large, irregular particles are Cr_2S_3. A high-magnification image of the spalled region (Fig. 6c) shows the presence of oxides and pores embedding in the alloy matrix where the initial B2 phase was. $Al_{1.0}$ and $Al_{1.3}$ show similar surface morphologies (Fig. 6c and 6 g). The oxide layers are both clean and dense (Fig. 6e and h); the spalled regions show uniaxial grains with randomly distributed Cr_2S_3 grains and pores smaller than 1 μm.

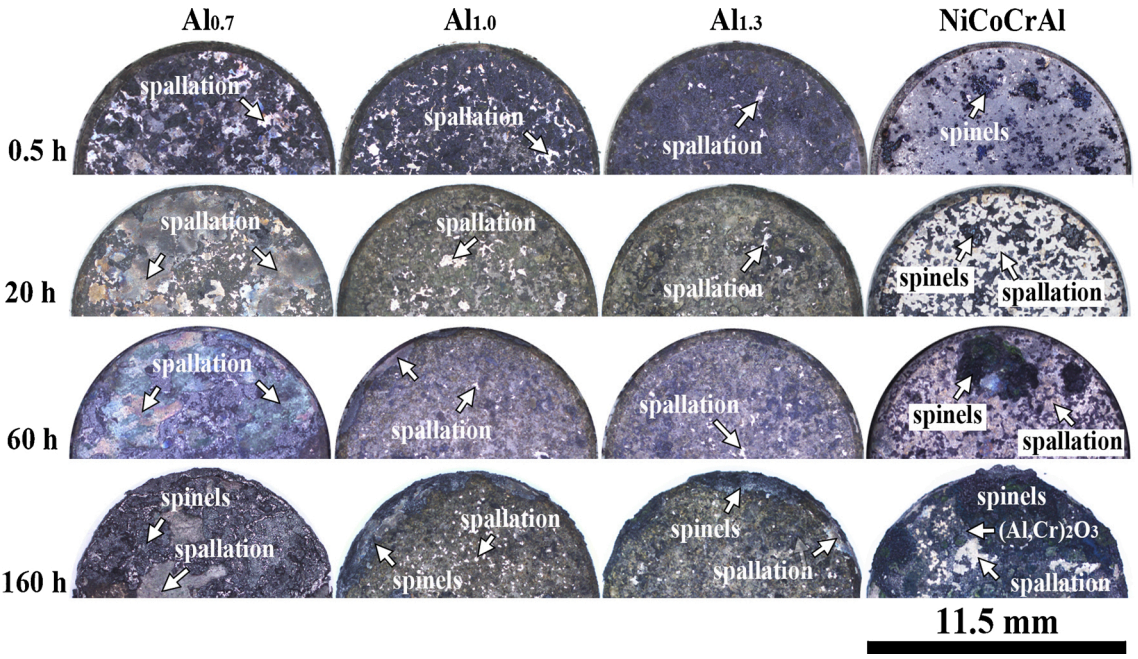

Fig. 2. Optical macrographs of the four alloys after hot corrosion at 900 °C under Na_2SO_4 +25 % NaCl molten salts film for different times.

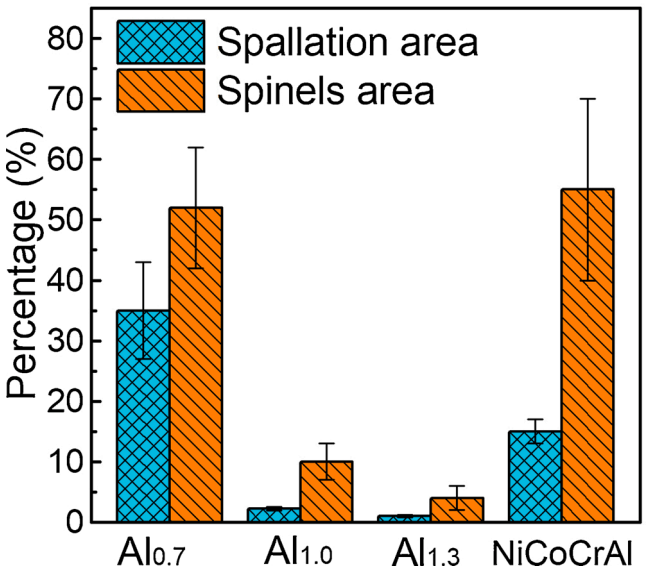

Fig. 3. Respective ratios of spallation and spinel to the whole surface for the four alloys after 160 h hot corrosion.

NiCoCrAl shows very different surface morphology after 0.5 h hot corrosion (Fig. 6j). The most noticeable feature is the presence of site-specific oxidation, that is, dark oxides on the β phase are rich in Al and grey oxides on the γ phase are rich in Cr. A high-magnification image of the oxide scale shows dense and uniform grains (Fig. 6k), whereas that of the spalled region (Fig. 6l) shows a site-specific corrosion of the matrix, in which connected pores around β phase and internal pores formed in β phase can be observed, whereas γ phase retains good integrity. The bare metal showed uneven morphology (Fig. 6(f)(i)(l)), which may be caused by different corrosion rates on different crystal orientations [27].

3.4. Surface morphologies after 160 h exposure

Surface morphologies adjacent to the boundaries of scale/spalled region after 160 h hot corrosion are shown in Fig. 7. $Al_{0.7}$ and NiCoCrAl show complex corrosion products besides Al_2O_3 and Cr_2O_3, that is, Fe_3O_4 and $CoFe_2O_4$ for $Al_{0.7}$ in Fig. 7(a)(b), and $(Ni,Co)(Al,Cr)_2O_4$ for NiCoCrAl in Fig. 7(j)(k). These loose corrosion products have weak bonding with the matrix and no protection to the alloys from hot corrosion and oxidation. On the contrary, $Al_{1.0}$ and $Al_{1.3}$ have relatively integrated scales. They show similar morphologies for both oxides and spallation regions, as shown in Fig. 7d-f for $Al_{1.0}$ and Fig. 7g-i for $Al_{1.3}$. $Al_{1.3}$ shows less spallation as well as a smaller number of warped oxide than $Al_{1.0}$.

Apart from the oxide scales, the spalled regions of the four alloys also show distinct morphologies after 160 h hot corrosion. For $Al_{0.7}$, as shown in Fig. 7c, large pores (~ 10 μm) can be observed and some are partially filled by Al_2O_3 clusters. For $Al_{1.0}$ and $Al_{1.3}$, oxide clusters smaller than 5 μm are randomly distributed in the alloy matrix (Fig. 7f and i). For NiCoCrAl, a large number of oxide particles form porous clusters, fill the cavities, and even protrude from the surface. The surfaces of bare metals are round and smooth due to the corrosion by the molten salts. From the morphologies of the bare metals, molten salts are more likely to infiltrate $Al_{0.7}$ and NiCoCrAl through big pores and cavities filled with the non-protective porous oxides clusters.

3.5. Cross-sectional microstructure and element profiles after corrosion

Fig. 8 shows the cross-sectional BSE micrographs and the EDS mapping of O and S of the four alloys. The penetration depths of O and S suggest the attack depths by the molten salts. All the four alloys show internal attacks with different depths and Al-poor zone beneath the interface. The specific attack depths of the four alloys after 160 h hot corrosion are listed in Table 3. NiCoCrAl has the worst inner oxidation and sulfidation deeply into the matrix, whose corroded depth is the largest, reaching 135 μm, while corrosion products in HEAs are few and the corrosion depths are shallow. $Al_{0.7}$ has a medium corroded depth about 75 μm, but considering its catastrophic oxidation and spallation, the corroded zone is relatively new in each corrosion cycle compared to the other three. The distribution of oxides in $Al_{0.7}$ is mainly along with the interfaces of B2/A1 phases marked by black arrows in Fig. 8a. Both $Al_{1.0}$ and $Al_{1.3}$ have shallow corroded depths, not more than 50 μm. The depths in HEAs decrease with the increasing Al concentration.

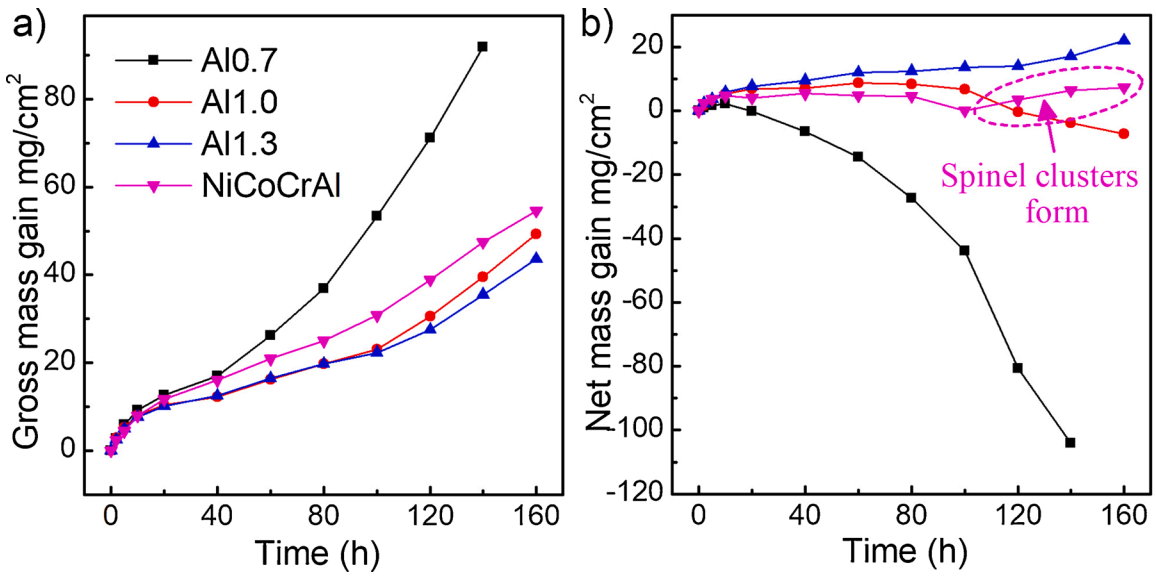

Fig. 4. Cyclic hot corrosion kinetic curves of the four alloys at 900 °C under Na_2SO_4 +25 % NaCl molten salts film: (a) the gross mass gain (the total mass change of the samples including the spallations); (b) the net mass gain (only the sample mass change excluding the mass of spallations).

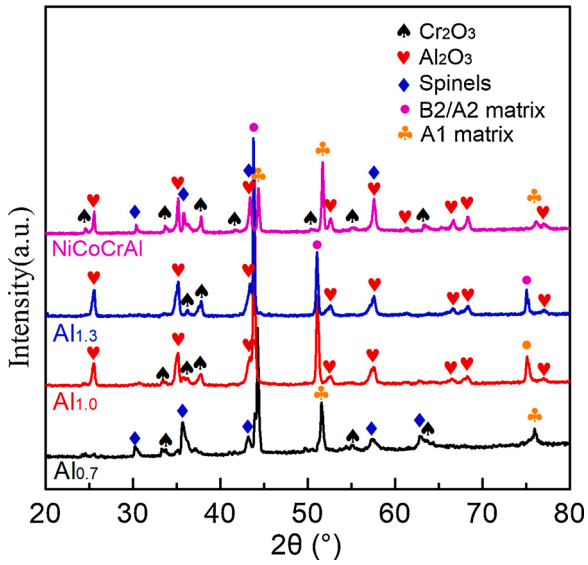

Fig. 5. XRD patterns of the four alloys after hot corrosion for 160 h at 900 °C under Na_2SO_4 +25 % NaCl molten salts.

Consumption of Al causes an uphill diffusion of Cr from the matrix towards the corrosion front because lower Al concentration decreased the Cr activity [28,29]. The Al-poor zone in $Al_{1.3}$ possesses enriched Cr concentration, forming a Cr reservoir on the top of the matrix shown as Fig. 9. A CrS layer forms on the surface of this zone. EDS analyses of the phase-transformed Al-poor zones in four alloys are listed in Table 4, from which the Al concentrations in HEAs are only half of the that in NiCoCrAl. This is a significant advantage because a lower equilibrium Al concentration meant that Al is better utilized to resist hot corrosion. The Cr content are also noteworthy, they increase from $Al_{0.7}$ to $Al_{1.3}$, and the contents of Cr in $Al_{1.0}$ and $Al_{1.3}$ are higher than NiCoCrAl, which is beneficial to resist the basic fluxing. But to $Al_{0.7}$, which has the lowest Cr content while possesses the highest initial Cr content as shown in Table 1.

The semi-quantitative elemental profiles of S, O, and Na deep into the matrix by GD-OES in $Al_{1.3}$ and NiCoCrAl after 160 h are shown in Fig. 10. The penetration depths of all three elements are much larger in NiCoCrAl than in $Al_{1.3}$. Both the depth profiles O and Na in $Al_{1.3}$ are limited to 20 μm from Fig. 10a (O) and Fig. 10c (Na), while the depths in NiCoCrAl are 100 μm and beyond 150 μm respectively. The full-scale range of O is displayed in Fig. 10b. Detection of Na in the deep matrix and the decreased concentration with the increasing depth indicates a breakdown of the integrity of the NiCoCrAl matrix, and that the molten salts directly penetrate the matrix through capillarity action. Penetrate depth of O is two-thirds of Na, which suggests that the attack of the liquid molten salts is prior to gaseous air, and the molten salts act as a barrier to the oxygen from the air at high temperature. S has a deeper penetration depth and larger concentration than Na both in NiCoCrAl and $Al_{1.3}$ because of the diffusion. The concentration of S in NiCoCrAl reaches a peak at about 0.5 % at the depth of 80 μm, and penetration depth has beyond 170 μm in Fig. 10a. In $Al_{1.3}$, the existence of S is limited in 100 μm, but the concentration peak is at the scale/matrix interface then decreases shown as Fig. 10c, this meant sulfides exist at the interface and the reason will be discussed later. However, concentrations of S and Na in NiCoCrAl increase where the interface should be at the depth of 10 μm. The reason should be the absorption of the salts by pores and the existence of internal metal sulfides in the matrix. Furthermore, opposite concentration trends of the two alloys at the interface also suggest the breakdown of the matrix and the formation of the interconnected channels in NiCoCrAl.

4. Discussion

The major findings in this work show that $Al_{1.0}$ and $Al_{1.3}$ have superior hot corrosion resistance than $Al_{0.7}$ and NiCoCrAl. $Al_{1.0}$ and $Al_{1.3}$ show uniform planar corrosion and have less weight change and spallation, simple $(Al,Cr)_2O_3$ scale, smaller corroded pores in the matrix, and much shallow internal attacks. $Al_{0.7}$ experiences catastrophic corrosion, while NiCoCrAl has the deepest internal attacks and many spinel clusters on the surface, and both of them show phase interface attacks leading to deeper corrosion. The three different hot corrosion behaviors imply different corrosion mechanisms, and the superior hot corrosion resistance of AlCoCrFeNi HEAs will give us useful enlightenment. The following part focuses on exploring the possible mechanisms responsible for the superior hot corrosion resistance of $Al_{1.0}$ and $Al_{1.3}$.

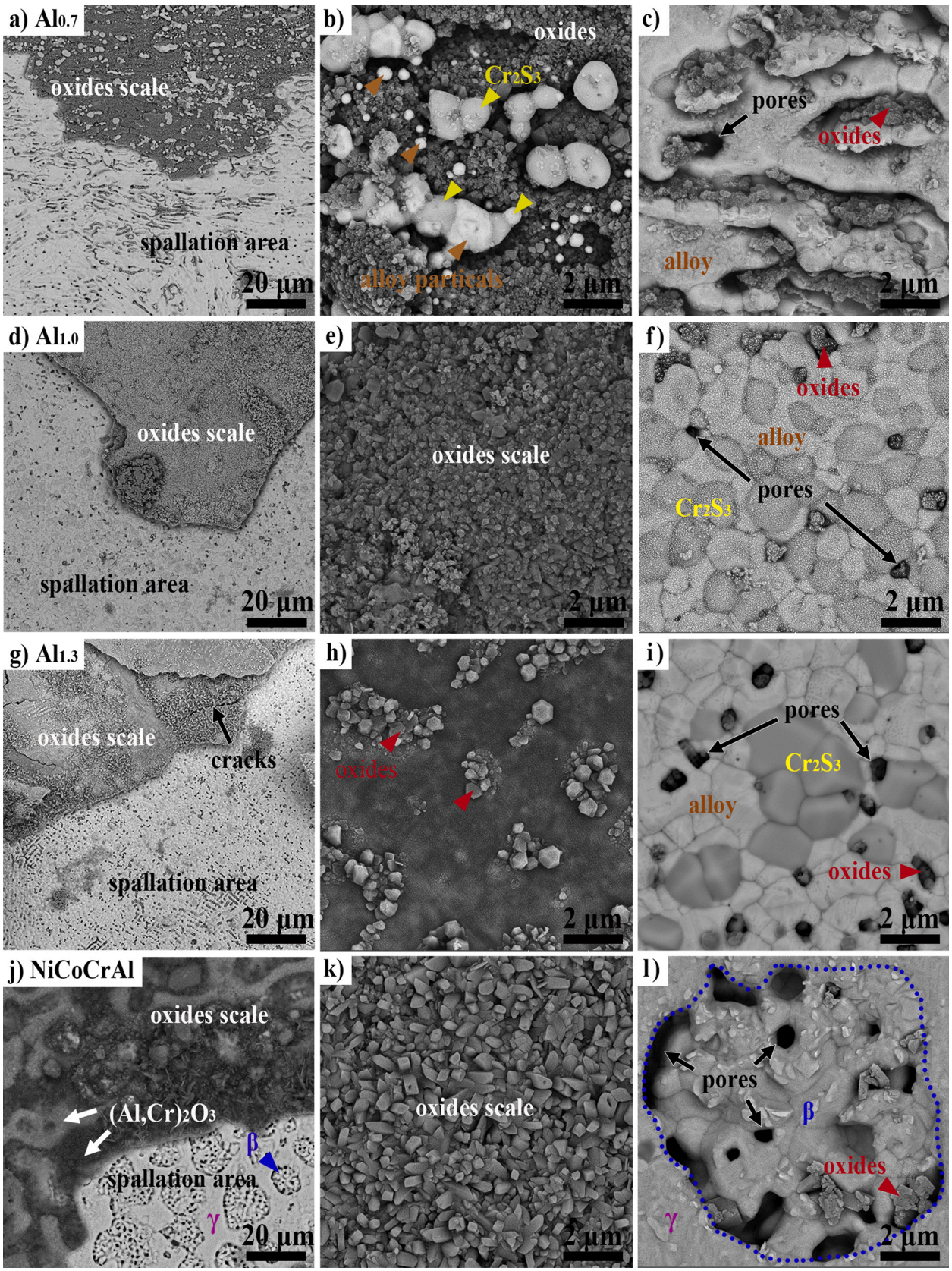

Fig. 6. BSE images of the surface morphologies of the alloys after 0.5 h hot corrosion at 900 °C under Na_2SO_4 +25 % NaCl molten salts focused on different areas: (a), (d), (g) and (i)the spallation edge of $Al_{0.7}$, $Al_{1.0}$, $Al_{1.3}$ and NiCoCrAl respectively; (b), (e), (h) and (k) the oxides scale of $Al_{0.7}$, $Al_{1.0}$, $Al_{1.3}$ and NiCoCrAl, respectively; (c), (f), (i) and (l) the corroded matrix of $Al_{0.7}$, $Al_{1.0}$, $Al_{1.3}$ and NiCoCrAl, respectively.

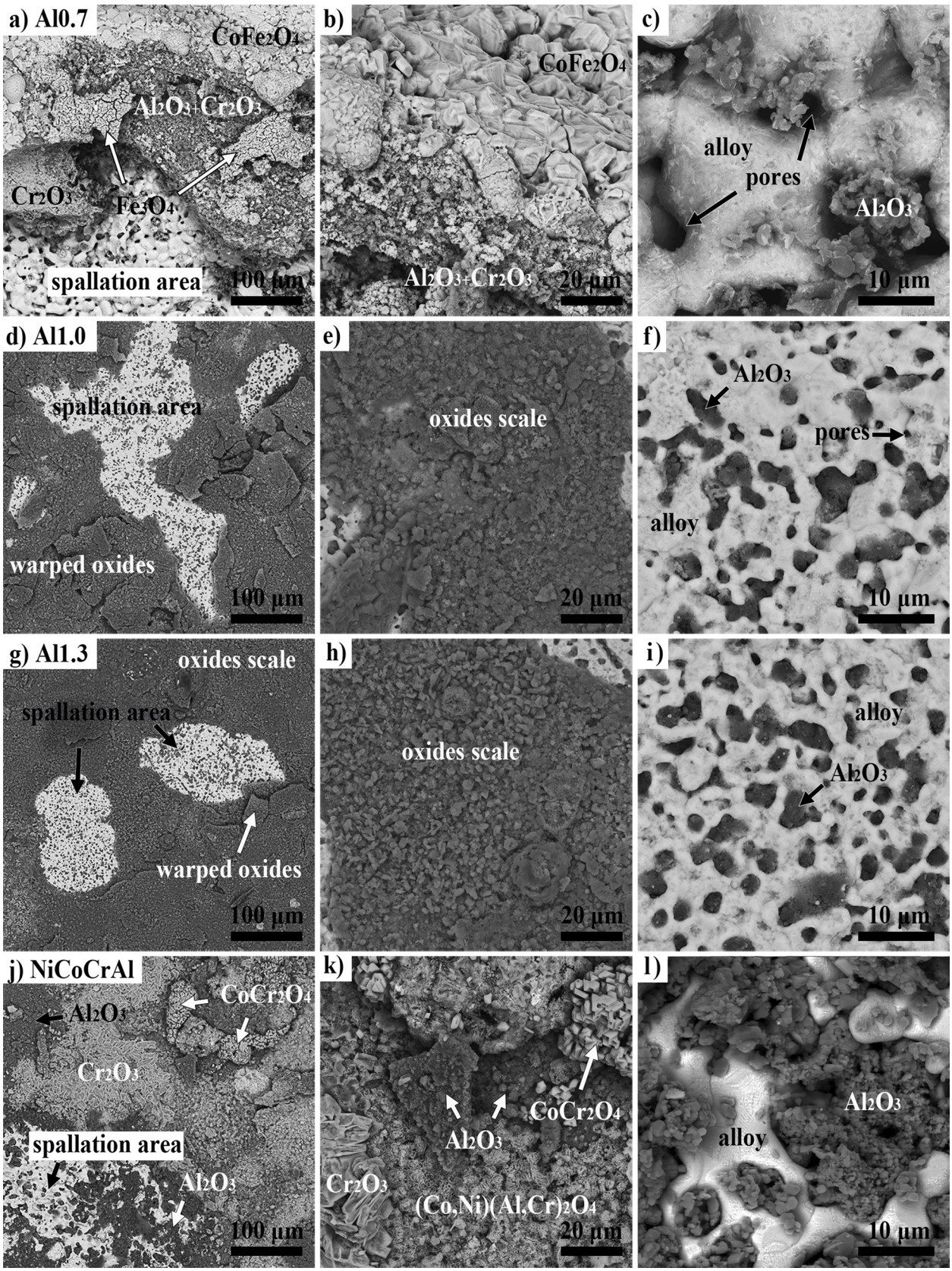

Fig. 7. Surface morphologies of the alloys after 160 h hot corrosion at 900 °C under Na_2SO_4 +25 % NaCl molten salts. (a), (d), (g) and (i) the spallation edge of $Al_{0.7}$, $Al_{1.0}$, $Al_{1.3}$ and NiCoCrAl respectively; (b), (e), (h) and (k) the oxides scale of $Al_{0.7}$, $Al_{1.0}$, $Al_{1.3}$ and NiCoCrAl, respectively; (c), (f), (i) and (l) the corroded matrix of $Al_{0.7}$, $Al_{1.0}$, $Al_{1.3}$ and NiCoCrAl, respectively.

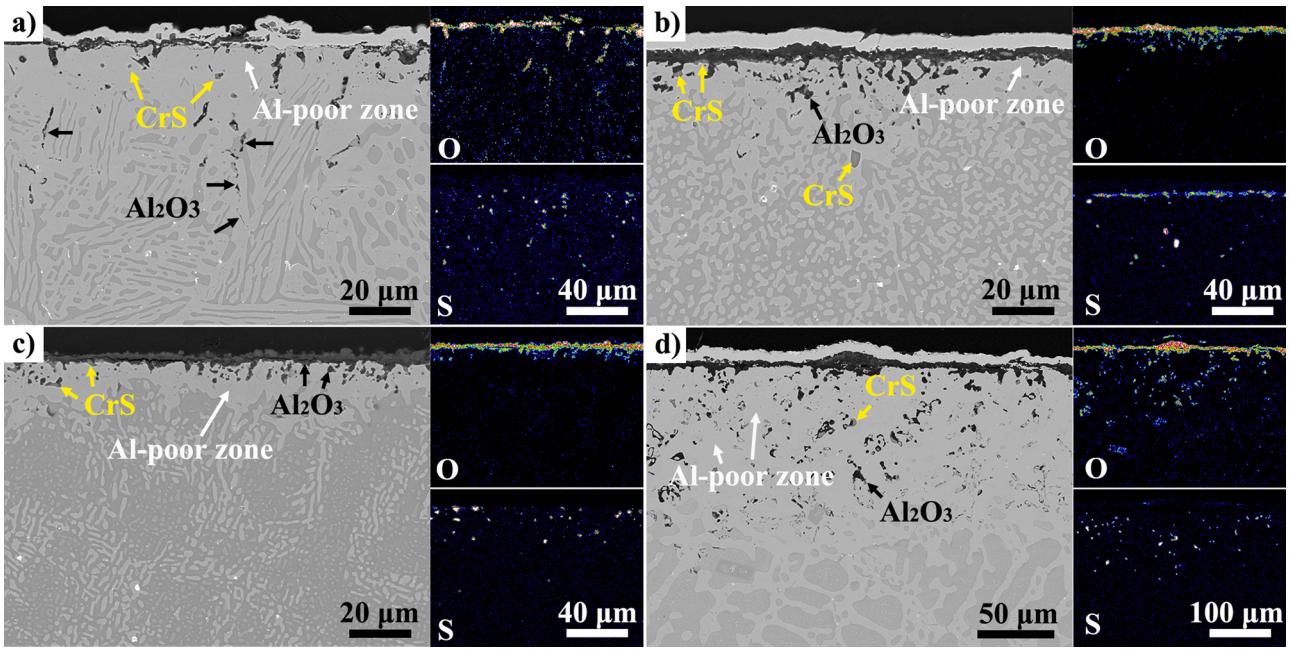

Fig. 8. Cross-sectional BSE micrographs and EDS mapping of S and O in the three HEAs and the NiCoCrAl alloy after 160 h hot corrosion: (a) $Al_{0.7}$; S and O penetrated the matrix along with B2/A1 phase interface. (b) $Al_{1.0}$; c) $Al_{1.3}$ and d) NiCoCrAl.

Table 3
Attack depths of O and S in four alloys after 160 h hot corrosion (μm).

Elements	$Al_{0.7}$	$Al_{1.0}$	$Al_{1.3}$	NiCoCrAl
O	65 ± 4	15 ± 5	10 ± 3	135 ± 7
S	75 ± 6	45 ± 6	25 ± 5	135 ± 9

4.1. Hot corrosion process

Compared to oxidation, the hot corrosion rate will increase about 200 times by alkali sulfate, and about 20000 times when the alkali chlorides are present causing scale blistering and spallation [30]. The electrochemical reaction in hot corrosion is complex when mix salts meet multi-component alloy, but the major reactions can be drawn with the help of thermodynamics.

4.1.1. Corrosion by chlorine

Mechanism of hot corrosion attack induced by sodium chlorides is termed as "active oxidation" or chlorine cycle" [30–32]. Generation of chlorine is described by the following reaction:

$$4Cl^- + O_2(g) = 2O^{2-} + 2Cl_2(g) \quad (1)$$

The released chlorine will diffuse through the porous scale and the molten salts, and then attack the alloy to form volatile metal chlorides at the scale/metal interface, where the oxygen activity is low. The reaction

Table 4
Chemical compositions of the Al-poor zone in four alloys after 160 h hot corrosion determined by SEM-EDS analysis (at %).

Materials	Elements (at %)				
	Al	Co	Cr	Fe	Ni
$Al_{0.7}$	4.7	27.1	18.3	24.9	25.0
$Al_{1.0}$	4.5	24.6	25.4	28.5	16.9
$Al_{1.3}$	4.3	24.0	26.3	31.8	13.6
NiCoCrAl	8.5	26.2	22.4	/	41.5

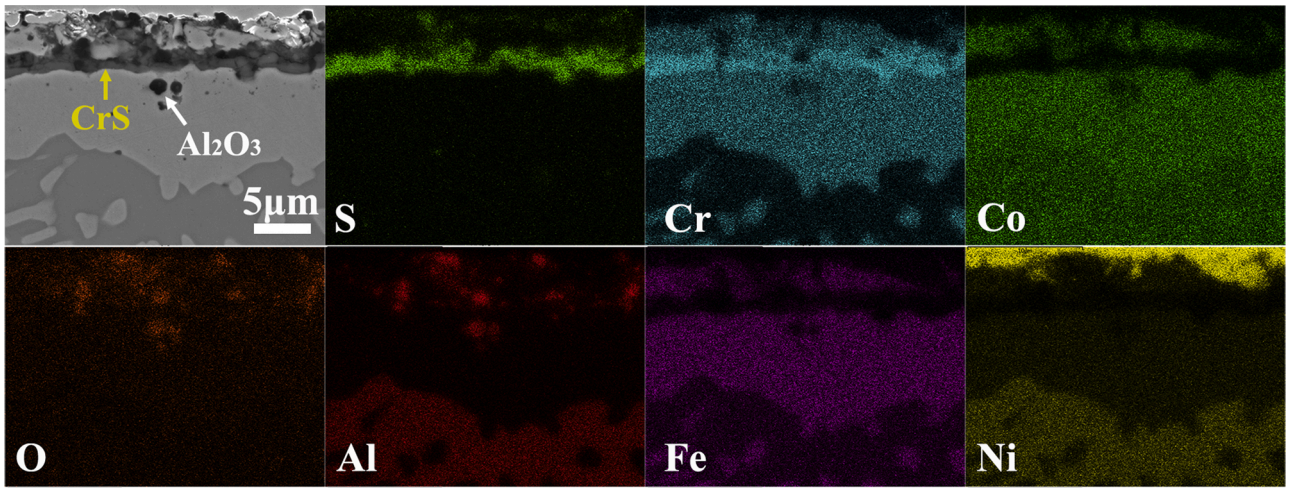

Fig. 9. BSE micrograph and corresponding EDS mapping of the corrosion front in $Al_{1.3}$ after hot corrosion under Na_2SO_4 + 25 % NaCl film at 900 °C.

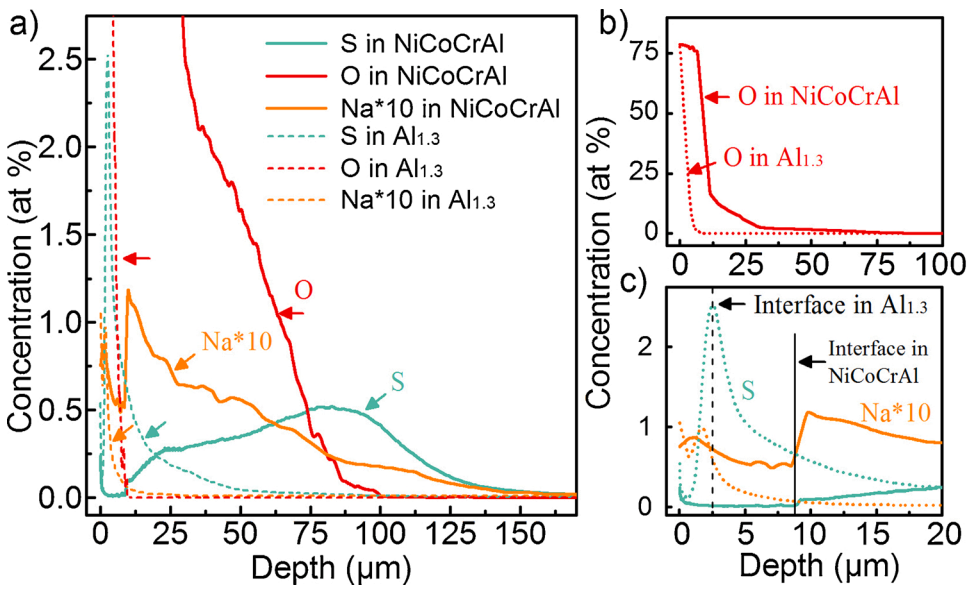

Fig. 10. The semi-quantitative depth profiles of S, O, and Na by GD-OES in $Al_{1.3}$ and NiCoCrAl after 160 h hot corrosion under Na_2SO_4 + 25 % NaCl film at 900 °C, the Na concentrations are magnified 10 times to make it easier to display: a) concentrations of S, O, and Na with an upper limit scale of 2.75 at % vs the depth to 170 μm, the concentration of O beyond the scale, but it is easier to know the attack depth of O in small scale range; b) concentrations of O in a full range in the depth of 100 depth μm; c) concentrations of S and Na in the depth limited to 20 μm to display the interface area more clear than the depth profiles in (a).

is described by:

$$M + Cl_2(g) \rightarrow MCl_x(g)\ (M = Al,\ Cr, etc.) \quad (2)$$

According to the standard Gibbs free energy of formation (ΔG_f^{θ}) at 1200 K ($AlCl_3$ (-347.1 kJ/(mol Cl_2) $^{-1}$, $CrCl_2$ (-252.4 kJ·(mol Cl_2)$^{-1}$, $CrCl_3$ (-207.1 kJ·(mol Cl_2)$^{-1}$, $FeCl_3$ (-101.6 kJ·(mol Cl_2)$^{-1}$, $CoCl_2$ (-145.3 kJ·(mol Cl_2)$^{-1}$, and $NiCl_2$ (-123.5 kJ·(mol Cl_2)$^{-1}$) [33], metal chlorides convert to metal oxides by reacting with oxygen at the gas/salts interface where the oxygen partial pressure (p_{O_2}) is sufficiently high:

$$AlCl_3 < CrCl_2 < CrCl_3 < FeCl_3 < CoCl_2 < NiCl_2$$

Therefore, chlorine reacts with Al selectively. When Al is consumed to a critical concentration, the reaction between chlorine and Cr becomes prior. Finally, other elements such as Fe, Co, and Ni are chloridized. A large amount of $AlCl_3$ volatilizes consuming Al and forms an Al-poor zone at the corrosion front. As oxides are more thermodynamically stable than their corresponding chlorides, that is, a lower standard Gibbs formation free energy (Al_2O_3 (-1295.0 kJ·mol^{-1}), Cr_2O_3(-826.0 kJ·mol^{-1})) [33], metal chlorides convert to metal oxides by reacting with oxygen at the gas/salts interface where p_{O_2} is sufficiently high:

$$MCl_x\ (g) + O_2(g) \rightarrow MO_y + Cl_2(g)\ (M = Al,\ Cr, etc.) \quad (3)$$

As the reactions progress, more and more chlorides formed at the metal/salts interface volatilize and gradually deposit at the salts/gas interface after oxidized, especially $AlCl_3$. As a result, a scale with large Al_2O_3 grains at the outer side forms as shown in Fig. 11. Thus, the chlorine regenerates, pass the scales, and attack the alloy again.

Unlike Al_2O_3, Cr_2O_3 is unstable and oxychloride is thermodynamically favored when oxygen and chlorine are both present. Volatile $CrO_2Cl_{2(g)}$ is the dominant species in Cr-O-Cl in a wide range of temperatures from 800 to 1600 K [6,34]. Volatilization of CrO_2Cl_2 will consume Cr_2O_3 at the scale/gas interface where the partial pressure of O_2 and Cl_2 are both higher:

$$Cr_2O_3 + 2Cl_2(g) + \frac{1}{2}O_2(g) = 2CrO_2Cl_2(g)\ \Delta G = 44060 - 13.2T\left(J \cdot mol^{-1}\right) \quad (4)$$

4.1.2. Corrosion by Na_2SO_4

When NaCl is consumed to a critical concentration, the corrosion progress comes into a stage that Na_2SO_4 plays a major role. The mechanism of the hot corrosion caused by Na_2SO_4 has been thoroughly investigated by previous studies [4,5]. The whole process can be described by Eq. (5) ~ Eq. (12). As the solubility of O_2 is low in the salts, transport of O_2 in the film is difficult when no SO_2/SO_3 exists in the atmosphere [35]. At the onset of hot corrosion, the sulfate ions dissociate into SO_3 and SO_3 further dissociates into sulfur and oxygen according to [36]:

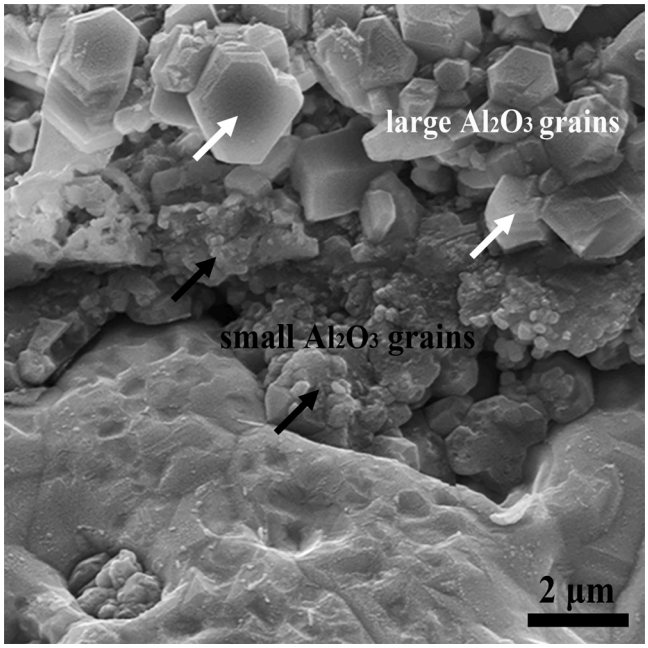

Fig. 11. The cross-view of the Al_2O_3 layer in $Al_{1.3}$ after 160 h hot corrosion at 900 °C under Na_2SO_4 +25 % NaCl molten salts film with small grains at the inner layer and large grains at the outer layer.

$$SO_4^{2-} = O^{2-} + SO_3 = O^{2-} + \frac{1}{2}S_2 + \frac{3}{2}O_2 \quad (5)$$

Oxidation and sulfidation of the active elements Al and Cr are described by Eqs. (6),(7) and Eqs. (8),(9), respectively. Al is the most affinitive to sulfur while Cr is the second, but due to the thermodynamic stability of Al_2O_3, CrSx is more stable than AlS_y at a certain p_{O_2} [37].

$$2Al + SO_3 = Al_2O_3 + \frac{1}{2}S_2\ \Delta G = -1035\ KJ \quad (6)$$

$$2Cr + SO_3 = Cr_2O_3 + \frac{1}{2}S_2 \ \Delta G = -557\ KJ \quad (7)$$

$$Al + S_2 \rightarrow AlS_y \quad (8)$$

$$Cr + S_2 \rightarrow CrS_x \quad (9)$$

The removal of O_2 and S_2 as Eq. (6) ~ Eq.(9) will lead to an increase in local basicity in the salt film adjacent to the matrix. As a result, basic fluxing of metal oxides will happen when the O^{2-} reaches a critical value as described by Eqs. (10)(11). However, to the dissolution of Cr_2O_3, the soluted species are CrO_2^- at low p_{O_2} as Eq. (11) and CrO_4^{2-} at high p_{O_2} as Eq. (12), and the solubility of Cr_2O_3 is higher at the salts/gas interface [38]. The condition results in a positive gradient of solubility of Cr_2O_3 in the salt film and eventually stopping the basic fluxing. The mechanism has been termed as Rapp-Goto criterion that continuous hot corrosion will happen when the solubility of oxides (C_{oxide}) is negative shown as Eq. (13) [4,5,39]:

$$Al_2O_3 + O^{2-} = 2AlO_2^- \quad (10)$$

$$Cr_2O_3 + O^{2-} = 2CrO_2^- \quad (11)$$

$$Cr_2O_3 + 2O^{2-} + \frac{3}{2}O_2 = 2CrO_4^{2-} \quad (12)$$

$$\left(\frac{dC_{oxide}}{dx}\right) < 0 \quad (13)$$

Another combined reaction with Cl_2 and SO_3 is shown as Eq. (14). $AlCl_3$ first forms by chloridation of Al in B2 β-NiAl then reacts with SO_3 and forms the low melting point Al·AlS_y eutectic [40,41]. The formation of AlS_y clusters shown in Fig. 12 supports this explanation. Once the liquid eutectic forms, the fast incursion at the phase interface occurs with the Al dissolution from the B2 β-NiAl phases. Simultaneously, Cr in A1 NiCoCr and A2 FeCr phases displaces the Al from the eutectic liquid forming CrS at the phase interface as Eq (15).

$$Al + AlCl_3 + ySO_3 = Al \cdot AlS_y + \frac{3y}{2}O_2 + \frac{3}{2}Cl_2 \quad (14)$$

$$Al \cdot AlS_y + yCr + \frac{3}{2}O_2 = yCrS + Al_2O_3 \quad (15)$$

Loose Al_2O_3 is the main corrosion product at the corrosion front, distributed where the B2 β-NiAl phase used to be, especially adjacent to the phase interface as shown in Al mapping and the inset in Fig. 12. This result suggests that the corrosion mainly exists in the B2 β-NiAl phase, and goes deeply into the matrix through phase boundaries and B2 β-NiAl phase. The formation of CrS + Al_2O_3 clusters marked by the yellow arrows and circles, and AlS_y + CrS_x + Al_2O_3 clusters marked by the white arrows in Fig. 12 support the reactions in Eqs. (14) and (15). Both the dissolution and the chemical reaction occurring at the phase interface lead to an accelerated attack.

4.2. High Al content and improved availability of Al in HEAs

Al plays the most important role to resist hot corrosion by the consumption of Cl_2 in the chloridation as Eq. (2) and forming Al_2O_3 scale, hence the total Al supply has a significant effect on corrosion resistance. Only $Al_{0.7}$ shows catastrophic corrosion because it has the lowest Al content and volume fraction of B2. Compared to NiCoCrAl, the HEAs possess lower equilibrium levels of Al concentration in the Al-poor layer and provide a more effective Al supply to resist the hot corrosion. The same results are also reported by Zhang et al. [40] by adding Fe in NiCoCrAlY coatings.

The Al concentrations for the three HEAs and NiCoCrAl are 14.9 %, 20.0 %, 24.5 %, and 22.5 % (Table 1) respectively in initial state, and the corresponding volume fraction of B2 phases, which has superior corrosion resistance to chloridation, are 35.8 %, 56.1 %, 73.3 %, and 57.9 % (Table 2). In general, the volume fraction of B2 phases increases with the increase of Al, resulting in better corrosion resistance. The Al concentrations drop to 4.5 %, 4.4 %, 4.2 %, and 8.5 % (Table 4) in the Al-poor zones after hot corrosion, thus the efficient Al concentrations are 10.4 %, 15.6 %, 20.3 %, 14.0 % respectively. $Al_{1.0}$ and $Al_{1.3}$ both have higher effective availability of Al, even though $Al_{1.0}$ has a lower initial Al concentration than NiCoCrAl, which gives a definite advantage over NiCoCrAl. $Al_{1.3}$ has a higher initial Al concentration and volume friction of B2 (17 % higher than in $Al_{1.0}$), but similar final Al concentration, leading to higher availability of Al than $Al_{1.0}$, and therefore less spallation and gross mass gain in Figs. 3 and 4.

Although the Al_2O_3 scales are loose on $Al_{1.0}$ and $Al_{1.3}$, they are also protective. At the interface of scale/matrix, where the oxygen potentials are low, the reverse reaction of Eq. (3) is favored [30]. $AlCl_3$ formed and diffusion toward the scale/gas interface where the p_{O_2} is high, re-oxidized to Al_2O_3, and deposited near the scale surface. As the volatilization and oxidation process go on, Al_2O_3 grains at the interface consume to smaller ones while forming larger grains near the top as shown in Fig. 11. The process results in the consuming of Cl_2 which generates from the molten salts or the chloridation-oxidation cycle, protecting the matrix from chloridation and hence reducing the

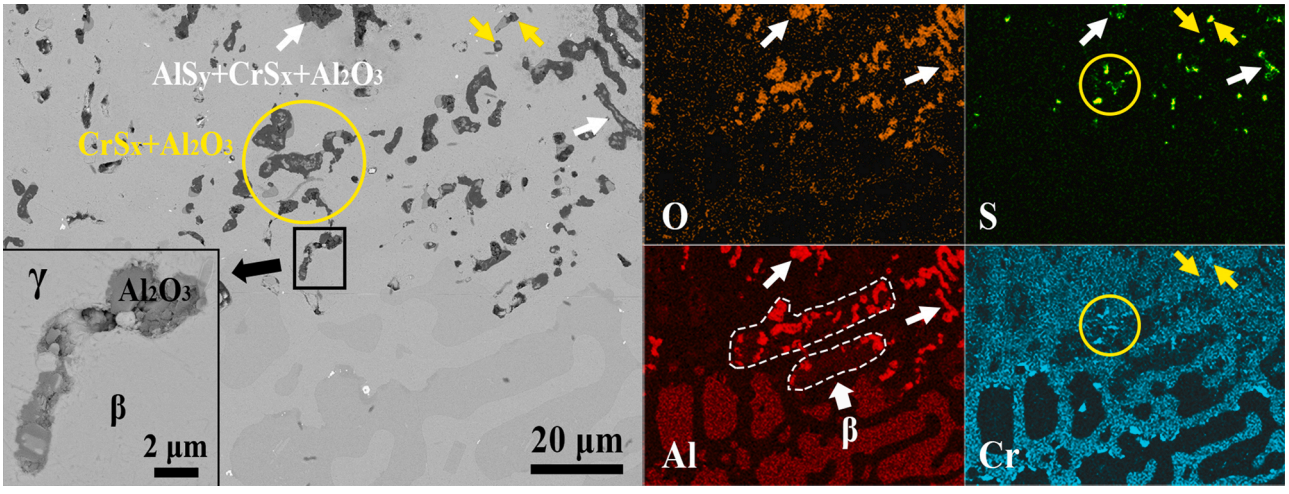

Fig. 12. BSE micrographs and EDS mapping at the corrosion front in the NiCoCrAl. Sulfides and oxides mainly distributed where the B2 β-NiAl phase used to be. The result suggests hot corrosion of NiCoCrAl is mainly through the corrosion of B2 β-NiAl phase.

depletion of the Al element.

4.3. Improved hot corrosion resistance by microstructures

The differences in corrosion behaviors between HEAs ($Al_{1.0}$ and $Al_{1.3}$) and NiCoCrAl are far more dramatic than the differences in Al contents and volume fractions of B2. The site-specific corrosion (Fig. 6c and l, Fig. 8a, and Fig. 12) in $Al_{0.7}$ and NiCoCrAl also indicates that microstructures influence the corrosion resistance significantly. The most severe selective corrosion in NiCoCrAl occurs at the phase interface, followed by the B2 β phase. This could be drawn from Fig. 6l, in which a continuous groove forms around B2 along B2/A1 interface.

4.3.1. Coherent phase interface

$Al_{0.7}$ with lamellar eutectic structure provides the through passages from the surface to the matrix, which gives the attack species Cl_2, SO_3, and S short-circuit diffusion paths and preferential attack sites for metal-sulfide eutectic liquid. But for modulated structures in $Al_{1.0}$ and $Al_{1.3}$, boundaries of isolated FeCr phases are loop-locked thus avoid fast attack through phase interfaces. Fig. 13a was a high-angle annular dark-field (HAADF) STEM image with corresponding energy-dispersive X-ray spectroscopy (EDS) maps of $Al_{1.3}$, in which the boundaries of B2/A2 phases are clear and closed.

The second one is the boundary type. For the eutectic $Al_{0.7}$, the phase interface is incoherent. But for the spinodally decomposed structure, the

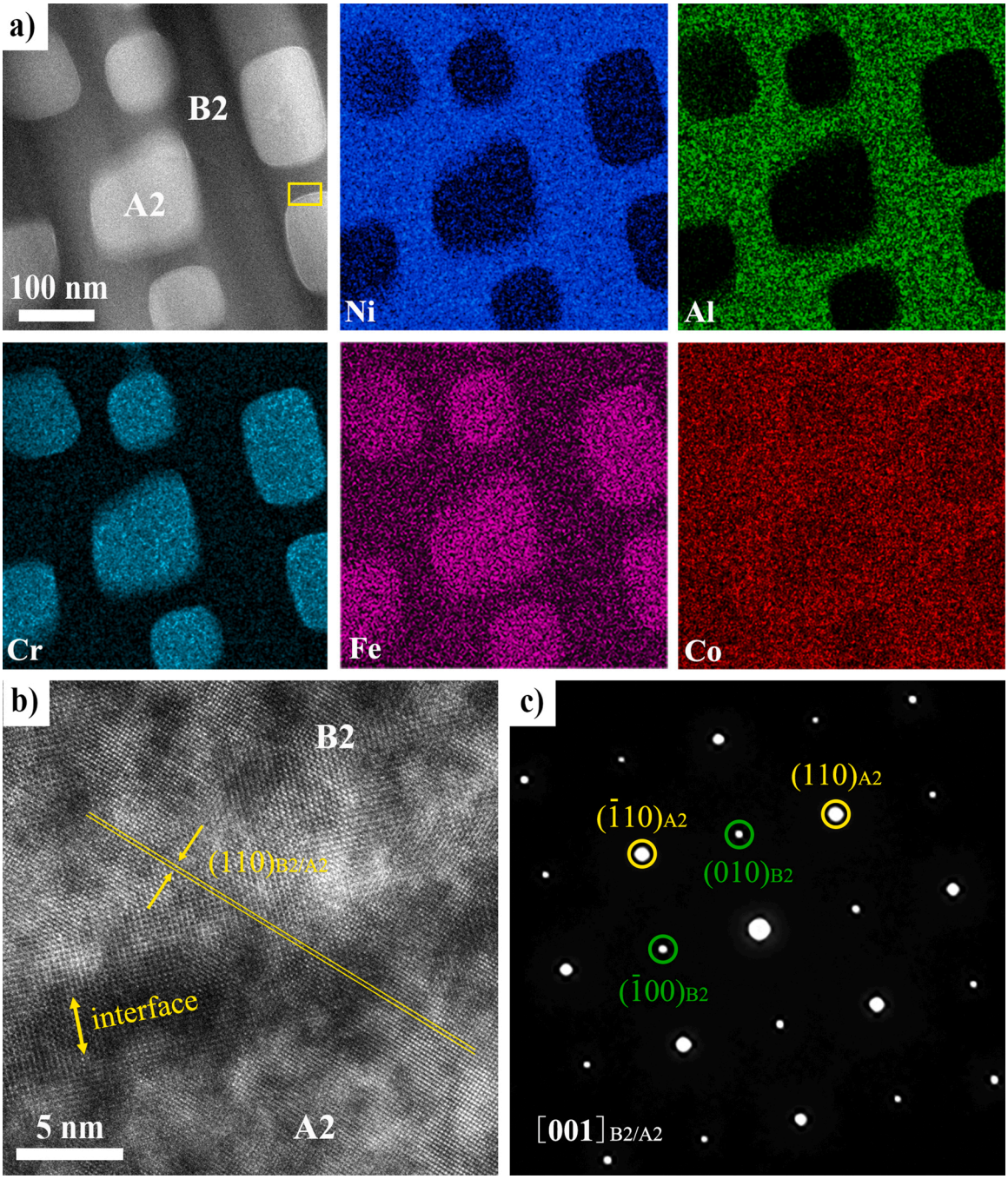

Fig. 13. TEM analysis of $Al_{1.3}$ HEA: a) high-angle annular dark-field (HAADF) STEM image with corresponding EDS mapping; b) high-resolution transmission electron microscopy (HRTEM) of B2/A2 interface marked by the yellow rectangle in (a) in [001] direction, the two phases are coherent; c) selected-area diff ;raction (SAD) patterns along [001] direction in the site of a) with a selected-area aperture of 800 nm.

phase boundary is coherent [42]. High-resolution transmission electron microscopy (HRTEM) and selected-area diffraction (SAD) were used to identify the orientation of the B2 and A2 phases. Fig. 13b shows the HRTEM image of the interface of B2/A2 marked by the yellow rectangle in Fig. 13a, and in this case the electron beam is parallel to <001> of the B2 and A2 phases. The atomic columns across the interface of B2/A2 are continuous and have a consistent orientation as marked in yellow lines, which indicates the B2 and A2 phases are coherent. Furthermore, SAD with a selected-area aperture of 800 nm where the whole area of Fig. 13a contained was conducted, therefore the diffraction area consisted of B2 base and many A2 phases. SAD patterns in Fig. 13c show the spots from B2 and A2 overlap completely, and super-lattice diffraction spots of B2 are marked with the green circle. Therefore, the interfaces in $Al_{1.3}$ are coherent with cube-on-cube orientation relationship, which have been observed in comparable structures in AlCoCrFeNi and AlCoCuCrFeNi HEAs of various concentrations of Al and Cr, whilst incoherent interface in $Al_{0.7}$ [20,43–45].

Therefore, corrosion species penetrate the $Al_{1.0}$ and $Al_{1.3}$ matrix through lattice diffusion, which is much slower than diffusion by phase interfaces containing many lattice defects [42]. Diffusion in solids can be described by the Arrhenius equation,

$$D = D_0 exp\frac{-Q_d}{RT} \quad (16)$$

where D is the temperature-dependent diffusion coefficients, D_0 is a temperature-independent preexponential, Q_d is the activation energy for diffusion, R is the gas constant, and T is the absolute temperature. The incoherent phase interface is similar to the high-angle grain boundary which has a much reduced Q_d and a much increased D_0 than the coherent interface [46].

The NiCoCrAl also has a multiphase structure consisting of coarse B2 β-NiAl and A1 γ-Ni phase with small needle-like γ and β phases precipitates respectively shown as Fig. 1d [47,48]. Numerous B2/A1 incoherent phase interfaces provide short-circuit diffusion paths for corrosion components, result in severe internal oxidation and sulfidation deeply into the matrix. As the internal attack goes severely, the internal channels form and provide penetrate paths not only to gas corrodents, but to molten salts, and therefore Na was detected deeply into the matrix in Fig. 10.

4.3.2. Phase size

Some researchers have reported the relationship between oxidation behaviors and the size of the phases in NiCoCrAl. Nijdam et al. [47] point out when β-NiAl phase sizes are larger than 20 μm, $NiCr_2O_4/Cr_2O_3$ outer layer above the inner α-Al_2O_3 will form on the top of γ-Ni phase; when β phase sizes are smaller than 3 μm a uniform and laterally homogeneous oxide will form on both β and γ phase. Luo et al. [49] and Chen et al. [50] also have reported that refinement of the microstructure is beneficial to reduce the threshold of Al concentration for the γ phase to form an exclusive Al_2O_3 scale due to fast β/γ boundary diffusion.

As to the hot corrosion, site-specific corrosion and oxidation occur throughout the process, which is more severe than the initial stage of oxidation in air, preventing the formation of a continuous and homogeneous Al_2O_3 scale. Therefore, the large phase size in arc-melting NiCoCrAl is detrimental to corrosion resistance. However, microstructure refinement cannot improve the corrosion resistance of NiCoCrAl either, because a large number of incoherent interfaces will be introduced, which is also detrimental to the corrosion performance. Regarding HEAs, both $Al_{1.0}$ and $Al_{1.3}$ have modulated phases with micron and submicron sizes and have the advantage of forming a uniform and homogeneous scale. Although the fine structure of $Al_{0.7}$ is conducive to form exclusive scale, the lowest Al content and lowest B2 fraction as well as the incoherent interface type lead to low resistance to hot corrosion.

$Al_{0.7}$ and NiCoCrAl show complex corrosion products and serious spallation compared with $Al_{1.0}$ and $Al_{1.3}$ from Fig. 2 and 3. The serious internal attack caused by the site-specific corrosion along the incoherent interface and low availability of Al leads to the breakdown of the alloy integrity, which reduces the contact area between the loose corrosion products and the matrix, thus resulting in serious scale spallation. In terms of $Al_{1.0}$ and $Al_{1.3}$, the integrity of the alloys maintain the bonding of the scale, and the small oxide intrusions act as pegs to increases the contact area, thus reducing the spallation.

The non-protective oxide products are more likely to spall off during cooling, leaving no protection against the molten salts. Thus, all the metal oxides could form under the high oxygen partial pressure, but NiO possesses the most rapid growth rate (a factor of ~10^4 faster than α-Al_2O_3) [51,52]. Then the spinel forms on the surface by the solid reaction between NiO and Al_2O_3/Cr_2O_3. On the contrary, for $Al_{1.0}$ and $Al_{1.3}$, loose scales infiltrated with molten salts maintain a low oxygen partial pressure at the scale/matrix interface, preventing the formation of spinel.

4.4. High Cr content in HEAs

Cr is effective in gettering sulfur released by Na_2SO_4 and stopping basic fluxing thus plays an important role in resisting the hot corrosion. At the one set of the corrosion for 0.5 h, Cr_2S_3 forms in $Al_{1.0}$ and $Al_{1.3}$ (Fig. 6), which suggests that a high SO_3 partial pressure which higher than p_{O_2} can establish in a short time from the phase stability diagram of Fig. 14a. No sulfides formed at the interface in $Al_{0.7}$ and NiCoCrAl due to

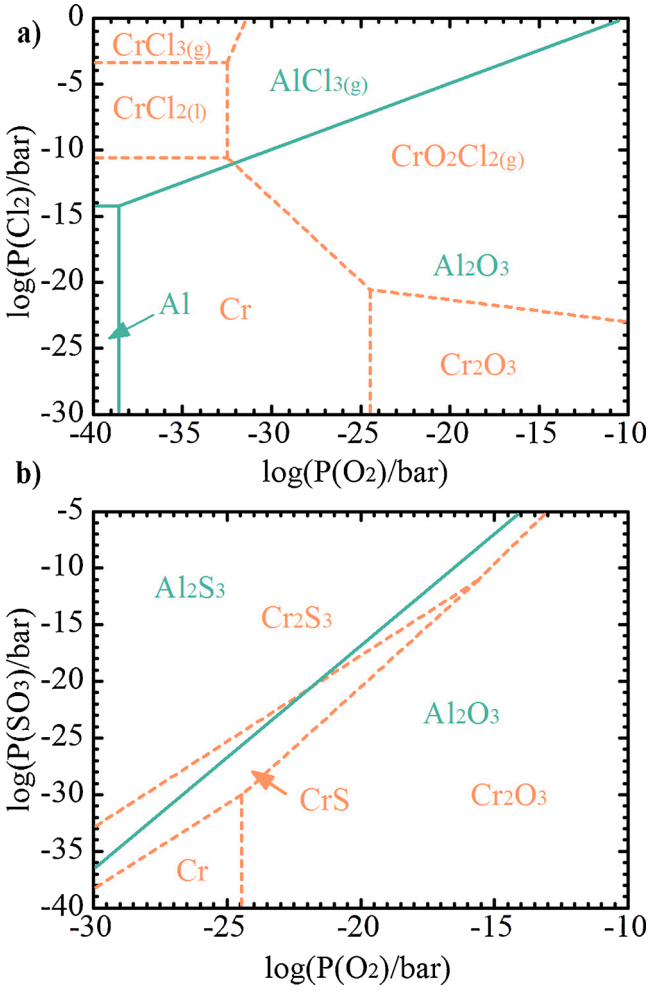

Fig. 14. Phase stability diagram at 900 °C of (a) (Al, Cr)-O-S; and (b) (Al, Cr)-O-Cl.

the damage of the matrix. After the hot corrosion test for 160 h, it is CrS, not Cr_2S_3, both at the interface and in the matrix. The results indicate molten salts can generate high SO_3 partial pressure, and keep a low O_2 partial pressure at the scale/matrix interface. As the corrosion time increases, the sulfur activity at the scale/matrix interface decreases due to the inward diffusion of sulfur, thus turning Cr_2S_3 to CrS which needs lower sulfur activity [53].

The Al-poor zone possesses enriched Cr concentration as high as 25.4 at % in $Al_{1.0}$ and 26.3 at % in $Al_{1.3}$ as shown in Table 4. When the salts are recoated on the surface, the newly formed Cl_2 is mainly consumed through forming volatile chloride or oxychloride with Cr, instead of Al due to the low Al concentration in the Al-poor layer. Oxychloride is thermodynamically favored when p_{Cl_2} and p_{O_2} are both increased, and then be oxidized when it moves outward where p_{O_2} increases but p_{Cl_2} decrease as shown in Fig. 14b. After NaCl is consumed, Na_2SO_4 also mainly reacts with Cr following the reaction process as Eq. (7)(9)(11)(12). Cr dissolves in molten salts as chromate by basic fluxing in the end. Therefore, when the hot corrosion process, Cr plays the most important role in consuming mixed molten salts. Due to the high Cr concentration in the Al-poor layer, S is trapped and captured to form a CrS layer on top of the matrix, and the diffusion depth is reduced by the Cr-rich layer. However, $Al_{0.7}$, which possesses the highest initial Cr content, has the lowest Cr concentration in the Al-poor zone. The reasons should be that the Cr plays a major role to resist the molten salts because of the initial shortness of Al, and the severe internal corrosion slows down the replenishment of Cr from the matrix.

The Cr contents in Pt-γ/γ', β-(Pt, Ni)Al, and NiCoCrAl are ~7 at % [54–56], ~5 at % [57,58], and 17 at % [50] respectively. High Cr content (> 19 at %) is one of the characteristics of AlCoCrFeNi HEAs compare with the existing bond coat materials.

5. Conclusion

The hot corrosion behaviors of $Al_xCoCrFeNi$ ($x = 0.7$, 1.0, and 1.3) HEAs against Na_2SO_4 + 25 % NaCl molten salts at 900 °C were investigated and compared to those of the traditional NiCoCrAl alloy. We found $Al_{1.0}CoCrFeNi$ ($Al_{1.0}$) and $Al_{1.3}CoCrFeNi$ ($Al_{1.3}$) with spinodally decomposed structure possess significantly enhanced hot corrosion resistance than $Al_{0.7}CoCrFeNi$ ($Al_{0.7}$) with eutectic lamellar structure and NiCoCrAl. The origin of the superior hot corrosion resistance of $Al_{1.0}$ and $Al_{1.3}$ is discussed both from the compositional and the microstructural viewpoints and the hot corrosion mechanism is proposed. These HEAs with tunable composition and microstructure, excellent oxidation and hot corrosion resistance, as well as good mechanical strength and coherent interface may have wide applications such as bond coat for thermal barrier coatings. The main conclusions are as follows:

(1) $Al_{1.0}$ and $Al_{1.3}$ HEAs show a significant improvement in hot corrosion resistance compare to NiCoCrAl. After hot corrosion for 160 h, the scales on $Al_{1.0}$ and $Al_{1.3}$ HEAs consist of $(Al, Cr)_2O_3$, but mainly $(Ni,Co)(Al,Cr)_2O_4$ clusters on NiCoCrAl. Elemental profiles by GD-OES show that molten salts and oxygen have penetrated the conventional NiCoCrAl deeply to 150 μm and 100 μm respectively, while a very shallow depth not more than 20 μm in $Al_{1.3}$.

(2) Aligned loop-locked coherent lattices of B2 β-NiAl and A2 FeCr phases with minimal defects hinder the diffusion of corrosion species, thus improving the hot corrosion resistance of the $Al_{1.0}$ and $Al_{1.3}$ HEAs. Incoherent phase interfaces provide short-circuit diffusion paths for corrosion components in $Al_{0.7}$ and NiCoCrAl.

(3) Al plays the major role to consume NaCl by forming $AlCl_3$, and finally forms Al_2O_3 scale on the $Al_{1.0}$ and $Al_{1.3}$; Cr hinders the hot corrosion by forming volatile chloride/oxychloride and CrS at the scale/matrix interface. Improved availability of Al and high Cr content in HEAs, as well as uniform distribution of Al and Cr in $Al_{1.0}$ and $Al_{1.3}$ result in a uniform planar and shallow attack, while the large phase in NiCoCrAl leads to site-specific corrosion in B2 β-NiAl, which in turn forms interconnected channels, further exacerbating internal corrosion.

The findings of this work offer a new strategy to design materials that are resistant to hot corrosion by varying the content of Al and Cr in a wide range in HEAs, which enables to adjust both the composition and the microstructure to balance the resistance of oxidation and hot corrosion, and mechanical properties for high-temperature applications.

Data availability

The raw/processed data required to reproduce these findings can be shared upon reasonable requests.

CRediT authorship contribution statement

Ling Li: Conceptualization, Methodology, Investigation, Data curation, Formal analysis, Writing - original draft. **Jie Lu:** Resources, Validation, Writing - review & editing. **Xuanzhen Liu:** Resources, Methodology. **Tao Dong:** Methodology, Writing - review & editing. **Xiaofeng Zhao:** Supervision, Conceptualization, Visualization, Project administration, Funding acquisition, Writing - review & editing. **Fan Yang:** Visualization, Project administration, Writing - review & editing. **Fangwei Guo:** Methodology, Formal analysis.

Declaration of Competing Interest

The authors report no declarations of interest.

Acknowledgments

The authors would acknowledge the financial support from the National Science and Technology Major Projects of China (2017-VI-0011-0083) and the National Natural Science Foundation of China (No. 51971139).

References

[1] J.R. Nicholls, Advances in coating design for high-performance gas turbines, MRS Bull. 28 (2003) 659–670.
[2] N. Eliaz, G. Shemesh, R.M. Latanision, Hot corrosion in gas turbine components, Eng. Fail. Anal. 9 (2002) 31–43.
[3] F. Pettit, Hot corrosion of metals and alloys, Oxid. Met. 76 (2011) 1–21.
[4] N. Birks, G.H. Meier, F.S. Pettit, Introduction to the High Temperature Oxidation of Metals, Cambridge University Press, 2006.
[5] D.J. Young, Chapter 8 - Corrosion by sulphur, in: D.J. Young (Ed.), High Temperature Oxidation and Corrosion of Metals, second edition, Elsevier, 2016, pp. 393–430.
[6] D.J. Young, Chapter 12 - corrosion in complex environments, in: D.J. Young (Ed.), High Temperature Oxidation and Corrosion of Metals, second edition, Elsevier, 2016, pp. 603–645.
[7] R.C. Reed, The Superalloys: Fundamentals and Applications, Cambridge university press, 2008.
[8] Q.M. Wang, Y.N. Wu, P.L. Ke, H.T. Cao, J. Gong, C. Sun, L.S. Wen, Hot corrosion behavior of AIP NiCoCrAlY(SiB) coatings on nickel base superalloys, Surf. Coat. Technol. 186 (2004) 389–397.
[9] H. Mei, Y. Liu, L. Cheng, L. Zhang, Corrosion mechanism of a NiCoCrAlTaY coated Mar-M247 superalloy in molten salt vapour, Corros. Sci. 55 (2012) 201–204.
[10] X. Liu, Y. An, X. Zhao, S. Li, W. Deng, G. Hou, Y. Ye, H. Zhou, J. Chen, Hot corrosion behavior of NiCoCrAlYTa coating deposited on Inconel alloy substrate by high velocity oxy-fuel spraying upon exposure to molten V2O5-containing salts, Corros. Sci. 112 (2016) 696–709.
[11] J.X. Chang, D. Wang, X.G. Liu, L.H. Lou, J. Zhang, Effect of rhenium addition on hot corrosion resistance of Ni-Based single crystal superalloys, Metall. Mater. Trans. A 49 (2018) 4343–4352.
[12] J. Sun, S.B. Liu, W. Li, H.J. Yu, S.M. Jiang, J. Gong, C. Sun, Hot corrosion behaviour of Pt modified aluminized NiCrAlYSi coating on a Ni-based single crystal superalloy, Corros. Sci. 149 (2019) 207–217.
[13] J.R. Nicholls, N.J. Simms, S. Neseyif, H.E. Evans, C. Ponton, M. Taylor, Hot corrosion of smart overlay coatings, High Temperature Corrosion and Materials Chemistry Electrochemical Society Proceedings (2000) 270–281.

[14] J. Wang, M. Chen, Y. Cheng, L. Yang, Z. Bao, L. Liu, S. Zhu, F. Wang, Hot corrosion of arc ion plating NiCrAlY and sputtered nanocrystalline coatings on a nickel-based single-crystal superalloy, Corros. Sci. 123 (2017) 27–39.
[15] Z.B. Bao, Q.M. Wang, W.Z. Li, X. Liu, J. Gong, T.Y. Xiong, C. Sun, Preparation and hot corrosion behaviour of an Al-gradient NiCoCrAlYSiB coating on a Ni-base superalloy, Corros. Sci. 51 (2009) 860–867.
[16] Y.P. Wang, B.S. Li, M.X. Ren, C. Yang, H.Z. Fu, Microstructure and compressive properties of AlCrFeCoNi high entropy alloy, Mater. Sci. Eng. A 491 (2008) 154–158.
[17] Y.-F. Kao, T.-J. Chen, S.-K. Chen, J.-W. Yeh, Microstructure and mechanical property of as-cast, -homogenized, and -deformed AlxCoCrFeNi (0≤x≤2) high-entropy alloys, J. Alloys. Compd. 488 (2009) 57–64.
[18] W.-R. Wang, W.-L. Wang, J.-W. Yeh, Phases, microstructure and mechanical properties of AlxCoCrFeNi high-entropy alloys at elevated temperatures, J. Alloys. Compd. 589 (2014) 143–152.
[19] T.K. Tsao, A.C. Yeh, C.M. Kuo, H. Murakami, High temperature oxidation and corrosion properties of high entropy superalloys, Entropy 18 (2016).
[20] T.M. Butler, M.L. Weaver, Oxidation behavior of arc melted AlCoCrFeNi multi-component high-entropy alloys, J. Alloys. Compd. 674 (2016) 229–244.
[21] T.M. Butler, J.P. Alfano, R.L. Martens, M.L. Weaver, High-temperature oxidation behavior of Al-Co-Cr-Ni-(Fe or Si) multicomponent high-entropy alloys, JOM 67 (2015) 246–259.
[22] J. Lu, Y. Chen, H. Zhang, N. Ni, L. Li, L. He, R. Mu, X. Zhao, F. Guo, Y/Hf-doped AlCoCrFeNi high-entropy alloy with ultra oxidation and spallation resistance, Corros. Sci. 166 (2020).
[23] J. Lu, Y. Chen, H. Zhang, L. Li, L. Fu, X. Zhao, F. Guo, P. Xiao, Effect of Al content on the oxidation behavior of Y/Hf-doped AlCoCrFeNi high-entropy alloy, Corros. Sci. 170 (2020), 108691.
[24] J. Lu, Y. Chen, H. Zhang, L. He, R. Mu, Z. Shen, X. Zhao, F. Guo, Y/Hf-doped Al0.7CoCrFeNi high-entropy alloy with ultra oxidation and spallation resistance at 1200 °C, Corros. Sci. 174 (2020), 108803.
[25] S. Gangireddy, B. Gwalani, V. Soni, R. Banerjee, R.S. Mishra, Contrasting mechanical behavior in precipitation hardenable AlXCoCrFeNi high entropy alloy microstructures: single phase FCC vs. Dual phase FCC-BCC, Mater. Sci. Eng. A 739 (2019) 158–166.
[26] H.J. Grabke, D.B. Meadowcroft, Guidelines for Methods of Testing and Research in High Temperature Corrosion, The Institute of Materials, London, 1995.
[27] X. Montero, A. Ishida, T.M. Meißner, H. Murakami, M.C. Galetz, Effect of surface treatment and crystal orientation on hot corrosion of a Ni-based single-crystal superalloy, Corros. Sci. 166 (2020), 108472.
[28] S. Salam, P. Hou, Y.-D. Zhang, H. Lan, H.-F. Wang, C. Zhang, Z.-G. Yang, Element accumulation beneath the scale/alloy interface of a CoNiCrAlReY alloy, Corros. Sci. 89 (2014) 318–325.
[29] N. Garimella, Y. Sohn, M. Brady, Interdiffusion in γ (face-centered cubic) Ni-Cr-X (X= Al, Si, Ge, or Pd) alloys at 900 C, J. Phase Equilibria Diffus. 27 (2006) 665–670.
[30] B.P. Mohanty, D.A. Shores, Role of chlorides in hot corrosion of a cast Fe–Cr–Ni alloy. Part I: Experimental studies, Corros. Sci. 46 (2004) 2893–2907.
[31] A. Zahs, M. Spiegel, H.J. Grabke, Chloridation and oxidation of iron, chromium, nickel and their alloys in chloridizing and oxidizing atmospheres at 400–700°C, Corros. Sci. 42 (2000) 1093–1122.
[32] R.A. Antunes, M.C.L. de Oliveira, Corrosion in biomass combustion: a materials selection analysis and its interaction with corrosion mechanisms and mitigation strategies, Corros. Sci. 76 (2013) 6–26.
[33] I. Barin, G. Platzki, Thermochemical Data of Pure Substances, 3rd ed ed., VCH, 1995.
[34] B.B. Ebbinghaus, Thermodynamics of gas phase chromium species: the chromium chlorides, oxychlorides, fluorides, oxyfluorides, hydroxides, oxyhydroxides, mixed oxyfluorochlorohydroxides, and volatility calculations in waste incineration processes, Combust. Flame 101 (1995) 311–338.
[35] R.A. Rapp, Y.-S. Zhang, Hot corrosion of materials: fundamental studies, JOM 46 (1994) 47–55.
[36] J.A. Goebel, F.S. Pettit, Na2SO4-induced accelerated oxidation (hot corrosion) of nickel, Metall. Trans. 1 (1970) 1943–1954.
[37] J.X. Chang, D. Wang, T. Liu, G. Zhang, L.H. Lou, J. Zhang, Role of tantalum in the hot corrosion of a Ni-base single crystal superalloy, Corros. Sci. 98 (2015) 585–591.
[38] R.A. Rapp, N. Otsuka, The role of chromium in the hot corrosion of metals, Electrochem. Soc. Trans. 16 (2009) 271–282.
[39] R.A. Rapp, K.S. Goto, The hot corrosion of metals by molten salts, ECS Proceedings Volumes 1981-10 (1981) 159–177.
[40] P. Zhang, X.-H. Li, J. Moverare, R. Lin Peng, The iron effect on hot corrosion behaviour of MCrAlX coating in the presence of NaCl at 900 °C, J. Alloys. Compd. 815 (2020), 152381.
[41] J. Ma, S.M. Jiang, J. Gong, C. Sun, Hot corrosion properties of composite coatings in the presence of NaCl at 700 and 900°C, Corros. Sci. 70 (2013) 29–36.
[42] D.A. Porter, K.E. Easterling, Phase transformations in metals and alloys (revised reprint), CRC press (2009).
[43] Y. Lu, X. Gao, Y. Dong, T. Wang, H.-L. Chen, H. Maob, Y. Zhao, H. Jiang, Z. Cao, T. Li, S. Guo, Preparing bulk ultrafine-microstructure high-entropy alloys via direct solidification, Nanoscale 10 (2018) 1912–1919.
[44] T.M. Butler, M.L. Weaver, Investigation of the phase stabilities in AlNiCoCrFe high entropy alloys, J. Alloys. Compd. 691 (2017) 119–129.
[45] B.A. Welk, R.E.A. Williams, G.B. Viswanathan, M.A. Gibson, P.K. Liaw, H.L. Fraser, Nature of the interfaces between the constituent phases in the high entropy alloy CoCrCuFeNiAl, Ultramicroscopy 134 (2013) 193–199.
[46] J.W. Christian, The Theory of Transformations in Metals and Alloys, Newnes, 2002.
[47] T.J. Nijdam, C. Kwakernaak, W.G. Sloof, The effects of alloy microstructure refinement on the short-term thermal oxidation of NiCoCrAlY alloys, Metall. Mater. Trans. A 37 (2006) 683–693.
[48] C. Leyens, I.G. Wright, B.A. Pint, Effect of experimental procedures on the cyclic, hot-corrosion behavior of NiCoCrAlY-Type bondcoat alloys, Oxid. Met. 54 (2000) 255–276.
[49] L. Luo, H. Zhang, Y. Chen, C. Zhao, S. Alavi, F. Guo, X. Zhao, P. Xiao, Effects of the β phase size and shape on the oxidation behavior of NiCoCrAlY coating, Corros. Sci. 145 (2018) 262–270.
[50] Y. Chen, X. Zhao, P. Xiao, Effect of microstructure on early oxidation of MCrAlY coatings, Acta Mater. 159 (2018) 150–162.
[51] F.H. Stott, G.C. Wood, J. Stringer, The influence of alloying elements on the development and maintenance of protective scales, Oxid. Met. 44 (1995) 113–145.
[52] B.A. Pint, A.J. Garratt-Reed, L.W. Hobbs, Analytical electron-microscopy study of the breakdown of α-Al2O3 scales formed on oxide dispersion-strengthened alloys, Oxid. Met. 56 (2001) 119–145.
[53] D.J. Young, W.W. Smeltzer, J.S. Kirkaldy, Nonstoichiometry and thermodynamics of chromium sulfides, J. Electrochem. Soc. 120 (1973) 1221.
[54] V. Deodeshmukh, N. Mu, B. Li, B. Gleeson, Hot corrosion and oxidation behavior of a novel Pt+Hf-modified γ′-Ni3Al+γ-Ni-based coating, Surf. Coat. Technol. 201 (2006) 3836–3840.
[55] Y. Zhang, J.P. Stacy, B.A. Pint, J.A. Haynes, B.T. Hazel, B.A. Nagaraj, Interdiffusion behavior of Pt-diffused γ+γ′ coatings on Ni-based superalloys, Surf. Coat. Technol. 203 (2008) 417–421.
[56] Y. Zhang, B.A. Pint, J.A. Haynes, I.G. Wright, A platinum-enriched γ+γ′ two-phase bond coat on Ni-based superalloys, Surf. Coat. Technol. 200 (2005) 1259–1263.
[57] Y. Zhang, J.A. Haynes, B.A. Pint, I.G. Wright, W.Y. Lee, Martensitic transformation in CVD NiAl and (Ni,Pt)Al bond coatings, Surf. Coat. Technol. 163-164 (2003) 19–24.
[58] J. Angenete, K. Stiller, Comparison of inward and outward grown Pt modified aluminide diffusion coatings on a Ni based single crystal superalloy, Surf. Coat. Technol. 150 (2002) 107–118.